X-ray micro-computed tomography for non-destructive 3D X-ray histology

Authors

Orestis L. Katsamenis[1*♦], Michael Olding[2+♦], Jane A. Warner[3], David S. Chatelet[2], Mark G. Jones[4], Giacomo Sgalla[4±], Bennie Smit[5], Oliver J. Larkin[5], Ian Haig[5], Luca Richeldi[4], Ian Sinclair[1,6], Peter M. Lackie[2,3], Philipp Schneider[1,7*]

** Corresponding authors*

♦ Orestis L. Katsamenis and Michael Olding contributed equally to this work

Affiliations

[1] µ-VIS X-Ray Imaging Centre, Faculty of Engineering and Physical Sciences, University of Southampton, UK

[2] Biomedical Imaging Unit, Clinical & Experimental Sciences, Faculty of Medicine, University of Southampton, Southampton General Hospital, Southampton, UK

[3] Academic Unit of Clinical and Experimental Sciences, Faculty of Medicine, University of Southampton, Southampton, UK

[4] National Institute for Health Research Respiratory Biomedical Research Unit, University Hospital, Southampton, Southampton, UK

[5] Nikon X-Tek Systems Ltd, Tring Business Centre, Icknield Way, HP23 4JX Tring, Herts, UK

[6] Engineering Materials Research Group, Faculty of Engineering and Physical Sciences, University of Southampton, Southampton, UK

[7] Bioengineering Science Research Group, Faculty of Engineering and Physical Sciences, University of Southampton, Southampton, UK

[+] current address: Nikon X-Tek Systems Ltd, Tring Business Centre, Icknield Way, HP23 4JX Tring, Herts, UK

[±] current address: Dipartimento di Scienze Cardiovascolari e Toraciche, Fondazione Policlinico Universitario A. Gemelli IRCCS, Rome, Italy

Supported by Wellcome Trust Pathfinder Award; grant number WT109682MA | M.G.J., I.H., L.R., I.S., P.M.L., P.S.

Conflict of interest

The authors have developed a novel µCT scanner (“Med-X”), optimised for soft-tissue image contrast. This technology development was a collaborative effort between Nikon X-Tek Systems (Tring, UK) and a partnership between the µ-VIS X-ray Imaging Centre at the University of Southampton and the Biomedical Imaging Unit (BIU) at the Southampton General Hospital.

Abstract

Historically, micro-computed tomography has been considered unsuitable for histological analysis of unstained formalin-fixed and paraffin-embedded (FFPE) soft tissue biopsies due to a lack of image contrast between the tissue and the paraffin. However, we recently demonstrated that µCT can successfully resolve microstructural detail in routinely prepared tissue specimens. Here, we illustrate how µCT imaging of standard FFPE biopsies can be seamlessly integrated into conventional histology workflows, enabling non-destructive three-dimensional (3D) X-ray histology, the use and benefits of which we showcase for the exemplar of human lung biopsy specimens. This technology advancement was achieved through manufacturing a first-of-kind µCT scanner for X-ray histology and developing optimised imaging protocols, which do not require any additional sample preparation. 3D X-ray histology allows for non-destructive 3D imaging of tissue microstructure, resolving structural connectivity and heterogeneity of complex tissue networks, such as the vascular or the respiratory tract. We also demonstrate that 3D X-ray histology can yield consistent and reproducible image quality, enabling quantitative assessment of tissue's 3D microstructures, which is inaccessible to conventional two-dimensional histology. Being non-destructive the technique does not interfere with histology workflows, permitting subsequent tissue characterisation by means of conventional light microscopy-based histology, immunohistochemistry, and immunofluorescence. 3D X-ray histology can be readily applied to a plethora of archival materials, yielding unprecedented opportunities in diagnosis and research of disease.

Introduction

Living tissues are multi-scale three-dimensional (3D) arrangements of cells and tissue matrices that constitute the fundamental building blocks of organs and organ systems. Imaging of such complex tissue architectures on a macroscopic and microscopic level is essential to elucidate their structure-function relationships and to understand the underlying tissue physiology and pathology. At a macroscopic level, where the whole body or large areas, such as whole organs, are of interest, imaging techniques such as clinical computed tomography (CT), magnetic resonance imaging (MRI) and ultrasound imaging allow for 3D, volumetric imaging. At the tissue and cellular level though, imaging is overwhelmingly constrained to two-dimensional (2D) examinations, with light microscopy being the dominant imaging technique for assessment of microscopic tissue structures.

Conventional 2D histology by light microscopy is employed to study tissue sections a few micrometres thick, which have been stained histochemically or immunohistochemically through chromogenic or fluorescent labelling. This allows specific tissue and cellular components to be identified and localised and is used to classify a wide range of tissue conditions and disease states. This can inform the stratification of patients for appropriate treatments, for instance for individuals suffering from idiopathic pulmonary fibrosis [1]. Formalin-fixed, paraffin-embedded (FFPE) tissues have been routinely prepared for 2D histopathological preparation since the end of the 19th century [2] and this approach remains the preponderant tissue preparation method. Although conventional histological analysis offers high spatial resolution down to a sub-cellular level, light microscopy of mechanically prepared thin sections can only provide 2D snapshots of the tissue structure. Tissue heterogeneities and structural interconnections are difficult to assess reliably. As a result, for any 3D spatial relationships to be inferred, multiple serial sections need to be cut, prepared, imaged and then reconstructed [3, 4], which often requires sophisticated image registration algorithms [5].

At microstructural or histological length scales (~1-100 µm), there is a lack of 3D analytical platforms that can resolve 3D spatial relationships for both hard and soft tissues. X-ray micro-computed tomography or microfocus computed tomography (µCT, micro-CT) is conceptually equivalent to medical CT, where hardware characteristics and arrangements are optimised for high spatial resolution (in the order of 1-100 µm), typically used for imaging material and tissue samples *ex vivo* and *in situ*, with typical sample dimensions in the order of mm to cm. In keeping with medical CT, µCT imaging is accomplished by placing the sample in the X-ray beam path and capturing projected X-ray absorption patterns (radiographs) over a large number of different rotation angles (typically hundreds to thousands). Contrary to medical CT, where the X-ray source and the detector rotate in a gantry system around the patient, in µCT systems, the X-ray source and detector are usually fixed in place and it is the sample that is rotated during image acquisition. Upon completion of a scan, CT reconstruction algorithms are employed to derive the X-ray absorption of the sample [6]. The technique was initially developed and optimised to image mineralised bone structures at a microscopic level [7] and since then, µCT is used routinely in many fields including archaeology [8, 9], biomedical research [10-17], engineering [18, 19], materials science [20, 21] and palaeontology [22, 23]. In the biomedical field, µCT has been successfully used over the last two decades to image biological tissues *ex vivo* [24-26]. Soft tissue imaging applications have also been reported, but these mostly rely on

laborious and intrusive sample preparation protocols that entail the use of X-ray attenuating stains (e.g. osmium tetroxide or iodine) [12, 25, 27, 28], complex X-ray optics systems [15] and/or synchrotron light sources [29, 30].

The fundamental challenge for accessible µCT imaging of routinely prepared soft tissues is the inherently low X-ray absorption contrast of these specimens [12, 25]. Mineralised tissues, such as bones and teeth, absorb a large fraction of the incident X-ray photons, resulting in good image contrast, even at typical hard X-ray energy levels offered by lab-based µCT systems (peak electrical potentials across the X-ray tube in the range of 20-200 kVp). In contrast, FFPE histology specimens of soft tissues or demineralised hard tissues, with inherently low X-ray attenuation contrast between the tissue and the supporting matrix (paraffin wax), have previously been considered beyond the reach of routine µCT imaging. As noted above, specialised sample preparation protocols and X-ray systems can be employed [12, 31, 32], associated with several important disadvantages. For instance, X-ray contrast agents often lack binding-specific affinity for different tissue types and rely on the diffusion of heavy ions (i.e. the contrast agent) into the tissue. The latter is a slow process that requires immersion of the tissue into the ions' solution, which can take up to several days to complete [32]. Also, spatial and temporal anisotropy of stains' penetration can result in artificial contrast gradients between the core and the surface of the tissue and in stain-induced shrinkage of the tissue sample [33-35]. This complicates the interpretation, segmentation and quantitative analysis of the microscopic tissue features of interest, such as epithelial surfaces, lymphatic vessels or colonic crypt foci. Moreover, many X-ray contrast agents preclude correlative imaging studies as they are incompatible with histochemical and immunohistochemical staining, or with techniques such as laser microdissection for subsequent nucleic acid analysis. Hence, tissue staining with X-ray contrast agents significantly limits practicality, sample availability and subsequent analysis with conventional histological methods. Most importantly, all staining protocols for X-ray imaging are disruptive to established histology workflows, as they are time consuming and add complication with the need for specialised and additional sample preparation protocols.

Recently, we have demonstrated that FFPE soft tissue samples, routinely prepared for light microscopy-based histology, can indeed be imaged non-destructively using conventional X-ray attenuation-based µCT without the need of any X-ray contrast agents. This was achieved by proposing a µCT imaging protocol at low X-ray fluxes and energy levels that exploits a modest X-ray attenuation contrast window between the soft tissue and the paraffin wax embedding medium [36, 37]. Initially applied to human lung surgical biopsies, the technique had allowed visualisation and segmentation of 3D structures [36] and provided sufficient image contrast for correlative identification and 3D localisation of fibroblastic foci in interstitial lung disease (ILD) [37], evidencing that non-destructive 3D imaging can be used to image soft tissue microstructures in health and disease. Specifically, Jones and co-workers demonstrated that fibroblastic foci in idiopathic pulmonary fibrosis are independent, discrete structures [37], in contrast to the previously proposed concept of an extended and interconnected fibroblast reticulum [38]. These studies highlight the potential of 3D tissue volume analysis by suitably optimised conventional µCT imaging to enhance pathological understanding and augment the value of correlated 2D imaging results from other histo(patho)logical methods.

In light of these recent steps forward, we developed a bespoke µCT scanner that is optimised for 3D imaging of unstained soft tissues. The new µCT system ("Med-X"; Nikon X-Tek Systems Ltd, Tring, UK) is designed for use in a medical/clinical environment and combines high-stability X-ray hardware with a high-efficiency detector, providing streamlined high-contrast imaging of routinely prepared soft tissue (i.e. standard FFPE blocks) at resolutions in the order of 5-10 µm (Figure 1). It is tailored to fit seamlessly into current histology workflows in biomedical and pre-clinical research, as well as clinical histopathology. We identify this framework as "3D X-ray histology". Here we apply *3D X-ray histology* to human lung biopsy specimens to demonstrate its promising potential for adding value to the conventional workflow of tissue analysis by (2D) light microscopy.

Materials and methods

Ethics

The study was performed in accordance with the University of Southampton's ethics policies and ethical guidelines. All samples were obtained with informed consent under full ethical approval (Mid and South Bucks Research Ethics Committee, MREC No. 07/H0607/73).

Human lung biopsies

Two representative human surgical lung biopsy specimens from clinically well-characterised patients with linked records, including clinical diagnosis, were used as exemplar model for the proposed soft tissue-optimised µCT approach for 3D X-ray histology. A control lung tissue sample was from macroscopically normal lung from a patient undergoing surgery for benign lung nodule resection. A diagnostic surgical lung biopsy sample had a typical usual interstitial pneumonia (UIP) pattern, confirmed by the independent review of two expert pulmonary pathologists, with the patient subsequently receiving a multidisciplinary diagnosis of idiopathic pulmonary fibrosis (IPF). All samples had received routine tissue processing for histology, including formalin fixation (in neutral buffered formalin) and paraffin embedding (FFPE), and subsequent mounting on standard histology cassettes (Figure 2). Typical lateral dimensions of embedded lung tissue biopsies were in the order of a centimetre, with a thickness in the millimetre range, specifically 11 mm × 7 mm × 3 mm for the control and 15 mm × 8 mm × 3 mm for the IPF sample.

µCT scanner for 3D X-ray histology

The authors have developed a novel µCT scanner ("Med-X"), optimised for soft-tissue image contrast. This technology development was a collaborative effort between Nikon X-Tek Systems (Tring, UK), and a partnership between the µ-VIS X-ray Imaging Centre at the University of Southampton and the Biomedical Imaging Unit (BIU) at Southampton General Hospital. The project was funded by a Wellcome Trust Pathfinder Award (grant number WT109682MA), which was focused on enhanced diagnosis and prognosis in ILD (2016-2017). The scanner was built to allow for stable, X-ray absorption-based imaging of unstained FFPE samples with dimensions used in standard clinical cassette mounts. The Med-X system was installed and commissioned in August 2016 at the Southampton General Hospital. The scanner is equipped with a 130 kVp multi-material target X-ray source and a high dynamic range 2000 × 2000 pixels flat panel detector.

µCT imaging protocol

To minimise interference of the cassette with the X-ray beam, FFPE lung tissue blocks were decoupled from the histology cassettes by removing excess wax from the back of the cassette and by carefully lifting off the specimen (Figure 2). This ensured that the tissue remained undisturbed and allowed for easy re-attachment of the wax block onto the cassette for further processing. The specimens were then placed into thin-walled stackable acrylic polymer cylinders (wall thickness ~1 mm) and stabilised with polyethylene foam (with negligible X-ray absorption) (Figure 2). To increase sample throughput, two cylinders were arranged on top of each other and scanned sequentially in a batch mode.

µCT imaging was conducted using a molybdenum target, the acceleration voltage was set at 55 kVp, while no X-ray pre-filtration was employed. The filament current was fixed at 125 µA (resulting in a filament power of 6.9 W), and the source-to-object and source-to-detector distances were set to 42.1 mm and 992.0 mm respectively, resulting in an isotropic voxel size of 8.48 µm. The experimental settings were adjusted to maximise the signal-to-noise ratio (SNR) and contrast-to-noise (CNR) ratio, while ensuring a sample throughput of two specimens per day (9.5 h scanning time per sample). 3501 projections were collected over an angular range of 360 degrees and 4 frames were averaged per projection to improve the SNR. Integration time per projection was set to 2 s and the detector's analogue gain to 24 dB.

Following µCT acquisition, the data were reconstructed to 32-bit raw volume files by means of Nikon's CT reconstruction software (CTPro, version V5.1.6054.18526; Nikon X-Tek Systems, Tring, UK) using conventional filtered back projection.

µCT data processing and calibration

Image pre-processing

The reconstructed 32-bit raw volumes were imported into Fiji/ImageJ (v1.51n) [39, 40], where a 3D median filter (1×1×1 kernel) was applied, followed by a 2D un-sharp mask (Gaussian blur factor = 2 pixels, applied on each reconstructed slice of the CT stack). Grey levels were linearly windowed to [-50, +100], containing the X-ray attenuation information of the soft tissue, paraffin wax and the surrounding air, and converted to 16-bit.

Image calibration

The 16-bit CT volumes were calibrated against a custom-made contrast phantom (calibration standard) containing standard histology-grade paraffin wax (Histology Wax, product number: 3808605E; Leica Biosystems), which was scanned using the same experimental settings prior to imaging of the actual samples. For this process, the histogram of the central CT slice (relative to the rotation axis) of each volume, containing soft tissue, paraffin wax and air, was analysed. The mean grey values corresponding to air and the wax were retrieved in both the actual sample and the phantom, and the two following factors were devised:

$$Contrast\ factor = \frac{(I_{wax} - I_{air})}{I_{wax}} \quad (1)$$

$$Calibration\ factor = \frac{Contrast\ factor_{phantom}}{Contrast\ factor_{sample}} \quad (2)$$

where I_{wax} and I_{air} in equation (1) are the mean grey values of the wax and the air, respectively.

The *Contrast factor* expresses the normalised grey value difference (i.e. the contrast) between the two known "materials" in a given scan, namely air and wax. The *Calibration factor* is a factor the CT data of the sample needs to be multiplied by, so that the contrast in the sample between air and wax matches the respective contrast in the phantom data. After this contrast calibration, the 16-bit grey values of the sample's CT data were linearly offset so that the mean value of air was assigned zero. The resulting calibrated CT volume was then saved as a single 16-bit tiff stack file for visualisation, further image processing and quantification.

Histology slides preparation

Following µCT image acquisition, FFPE tissue blocks were re-attached to their respective cassettes for routine histological processing. Sections 4 µm thick were then cut to a minimum depth of 80 µm into the tissue block and mounted on glass slides by following standard histology protocols. Finally, sections were deparaffinised and stained using haematoxylin and eosin (H&E) for later co-registration of the 2D (light microscopy-based) histology slide images with the µCT data.

Histology slide imaging, digitisation and co-registration with µCT data

Histology slides were imaged using a 20X objective on a dotSlide scanning system (VS110 Virtual Microscopy System; Olympus) and visualised using the proprietary VS Desktop software (v2.9; Olympus) and saved in the Olympus' native .vsi file format. The histology images were then imported in the visualisation and analysis software Amira (v6.1.1; Thermo Fisher Scientific) along with the corresponding µCT datasets. Plane correspondence between 2D histology sections and 3D µCT data was achieved by means of elastic landmark-based registration as follows: (i) Using the 2D histology image as a reference, a minimum of three landmark features contained in the histology slide were visually identified in the µCT volume; (ii) Because the wax blocks have been mounted parallel to the rotation axis of the µCT scanner (as shown in Figure 2), providing reconstructed CT data that is orthogonal to the data from standard histology, the µCT volume was resampled orthogonally to the plane defined by the landmarks using bicubic interpolation; (iii) Upon plane alignment, the CT slice, which matched best the corresponding histology slide, was visually identified, extracted and imported to Fiji/ImageJ (v1.51n) along with the histology image; (iv) The Fiji plugin *UnwarpJ* [41], an elastic registration method based on vector-spline regularisation [42], was applied to elastically register the histology image (warped source image) to the µCT slice (target image) to account for physical distortions caused during mechanical sectioning of the tissue block [43, 44].

Visualisation of correlative histology and µCT data

Co-registered µCT and histology data visualisation was performed in Amira (v6.1.1; Thermo Fisher Scientific). For this, the calibrated µCT volume was imported into the software along with the corresponding (co-registered) histology image. A clipping/cropping box was then applied to the µCT data to limit the field of view to 1.2 mm × 1.2 mm × 1.2 mm, allowing for a volumetric overview of the tissue microstructure. The µCT volume was windowed in such a way that only the soft tissue components were rendered, excluding air and paraffin wax. Additionally, maximum intensity projection (MIP) volume renderings, single slice and orthogonal slice

renderings were performed using Horos™ (v2.0.2)*, an open-source medical image viewer based on OsiriX™ (Pixmeo, Bernex, Switzerland). The "3D MIP" tool in Horos has been used to display the 3D volume, with "window width" and "window length" altered using the "Window Level Option" tool to highlight (X-ray) dense structures within the tissue. The same settings have been applied to all images presented here.

Quantification of tissue microstructural changes

Microstructural characteristics of the lung tissues were quantified using Fiji/ImageJ (v1.52d). For this, a mask was generated by manually tracing the boundary of the tissue and restricting the quantification to a volume of interest containing the tissue. Each volume was then binarised by absolute thresholding, using identical threshold grey values for both datasets, in order to segment (label) the voxels associated with the tissue and to separate them from the voxels in the volume associated with air or wax. The tissue's mean thickness and volume fraction were assessed using the "Thickness" and the "Volume Fraction" tools of the BoneJ plugin [45]. By definition, the tools assume that the studied structure (i.e. the segmented tissue) is assigned the foreground 8-bit grey-value (255) in the "binarised" image. The thickness of the structure is defined as a volume-weighed arithmetic mean of the local thickness distribution by fitting maximal spheres for all points within the structure, following the method by Hildebrand and Rüegsegger to assess thickness in 3D [46], where the local thickness at any given point of the structure is defined as the diameter of the largest sphere that contains this point and fits entirely within the structure. The volume fraction was calculated as the volume of the structure (i.e. the segmented tissue), divided by the mask (i.e. the volume of interest enveloping the tissue).

Results

Correlative imaging

Figure 3 shows a representative slice of the reconstructed 3D µCT dataset of the FFPE lung biopsy, taken from a non-involved site from a patient diagnosed with lung cancer, alongside the corresponding 2D H&E tissue histology slide. This side-by-side presentation of the µCT and histology data (cf. Supplementary Video 1) allows histology-guided identification of a range of tissue structures and diagnostically relevant histological criteria. In this example, key microstructural features such as small airways, blood vessels, and alveoli can be clearly seen in the µCT images and cross-referenced against the histological sections.

Once the 2D histology sections have been co-registered to the volumetric µCT data, both datasets were fused and could be displayed in a hybrid mode in 3D. This is shown in Figure 4, where the H&E-stained histology sections of the two lung biopsies were digitally interleaved with the corresponding tissue plane of the µCT volume and rendered along with the µCT data. Here, this rendering mode was used to demonstrate the microstructural differences between the control and the IPF tissue specimen.

µCT data visualisation

µCT data can be reviewed immediately following CT reconstruction, presented as an interactive image stack in which the viewer can browse through the depth of the specimen, zoom, pan, and perform basic dimensional

* https://horosproject.org

measurements (cf. Supplementary Video 2). Importantly, since µCT voxels (3D pixels) are isotropic, orthogonal planes of the µCT data can also be accessed immediately after CT reconstruction. This rendering mode, also known as multi-planar reconstruction (MPR), allows simultaneous imaging of virtual slices taken along the width, depth, and height of the specimen (Figure 5; top panel). Due to the isotropic voxel dimensions, virtual re-orientation and re-slicing of the specimen can be easily achieved *in silico* (Figure 5; bottom panel). An example of such an interactive assessment of the 3D data is shown in Supplementary Video 3, where the reviewer locates an airway and the corresponding blood vessel, examines the cross-sectional views along two orthogonal planes and proceeds to virtual re-orientation and re-slicing. By convention, we assign the "XY plane" to the plane that is parallel to the histology cassette (Figure 5; top panel). In this example (Figure 5; bottom panel and Supplementary Video 3; 00:37-onwards), rotation of the orthogonal axis viewing system along the Z- and X-axis (arrows) was performed to fully expose the longitudinal and transverse cross-sections of the blood vessel in the XY, and YZ/XZ planes, respectively.

An alternative and computationally inexpensive method to render volume data are maximum intensity projections (MIPs). MIP rendering is generated by an algorithm that casts rays of light through the dataset, where only the voxel with the highest X-ray attenuation (i.e. the brightest voxel) along each ray path is rendered [47]. Figure 6, Supplementary Video 4, and Supplementary Video 5 illustrate the ability to selectively discern features within a lung biopsy sample using the aforementioned MIP rendering method, applied on the µCT datasets.

Image quantification

Analysis of the tissue thickness showed that differences between the characteristics of the control and the IPF tissue biopsies could be identified. On average, the control lung tissue biopsy contained thinner structures (49.2 µm) than the IPF tissue biopsy (125.6 µm) (Figure 7). Volume rendering of the thickness map also shows greater heterogeneity in the IPF specimen, compared to the control (Figure 7 – left panel). In terms of volume fraction, the control sample had a smaller volume of lung tissue per unit volume of sample (33%) than the IPF sample (60%).

Stability of the µCT scanner

The µCT imaging and calibration protocol has been applied for over 30 lung biopsy samples (not shown here), resulting in consistent and reproducible image quality characteristics. Supplementary Figure 1 shows the histograms of nine specimens spanning a 3-month imaging period, along with the grey value variation for both the paraffin wax and tissue components of these specimens after grey value calibration. The graph demonstrates that fluctuation of the mean grey value for wax (= 30,419) was always less than 1% (standard error or SE = 284). The fluctuation of the mean grey value (= 40,289) for the tissue was higher but less than 2% (SE = 632), which is to be expected, given the electron density inhomogeneity of biological material.

Discussion

The study presented here is targeted at delivering a 3D visualisation solution for X-ray histology that is compatible with current histology workflows. It summarises the results of more than 3 years continuous

development of hardware technology as well as imaging and visualisation protocols & workflows since our first proof-of-principle µCT study on 3D imaging of paraffin-embedded human tissue samples [36]. The prototype µCT system we developed and used here ("Med-X"; Nikon X-Tek Systems Ltd, Tring, UK) represents a "distilled" version of its engineering "ancestor" (a heavy-duty walk-in 4.6 m × 2.4 m × 3.3 m experimental chamber used in our previous work [36]) and was specifically designed and optimised for use in a medical/clinical context and environment. Our study presents a detailed technical setup for 3D X-ray histology and establishes a detailed workflow specifically aligned with the use of paraffin-embedded tissue samples, which are routinely prepared for research or diagnostic applications. This includes assessment of equipment performance and stability over a period of several months, and critically includes a calibration procedure that establishes a baseline, which can serve as a standard for µCT imaging of soft tissues. This allows direct cross-sample and cross-scan comparisons, and in the future, also cross-site comparisons between different labs operating similar µCT systems. Briefly, calibrated 3D X-ray histology allows comparable 3D soft tissue µCT datasets to be generated over time and in different labs, and opens up tissue X-ray densities and microstructures to be scrutinised in a quantitative fashion.

X-ray attenuation-based µCT imaging of soft tissues without the use of any X-ray contrast agents is made possible through 3D X-ray histology. Direct comparison of the *de facto* standard for microstructural soft tissue analysis, namely 2D light microscopy-based histology, with 3D X-ray histology will be pivotal for the validation and adoption of the technique by histologists and histology laboratories. This approach is likely to be of particular value in conditions such as ILD where diagnosis is often challenging and pathological changes are dispersed and heterogeneous. The ability to identify the 3D location and extent of interstitial fibrosis and in particular fibroblastic foci within IPF samples using this approach has been demonstrated by Jones and colleagues [37]. Being able to review larger tissue volumes than is easily possible by conventional histology should facilitate the identification and assessment of spatial heterogeneity, patchy involvement of lung parenchyma and the presence of architectural distortion or microscopic honeycombing in ILD [48]. Using this non-destructive technique with standard FFPE samples opens up the possibility of applying soft tissue-optimised µCT in a clinically relevant context (Figure 1).

3D X-ray histology: visualisation modes and applications

Building on µCT studies of paraffin-embedded human tissue samples we published previously [36, 37] we discuss and demonstrate here a range of visualisation options for 3D X-ray histology using established medical image viewers. Our aim is to demonstrate the potential to visualise the information-rich 3D data of (human) tissue, displaying microstructures in more detail and in a way which is relevant to biomedical research and medical/clinical applications.

Distortion-free imaging and correlative 2D and 3D visualisation

Sectioning-induced defects, also referred to as "cutting", "preparation" or "histologic" artefacts, are a common problem encountered with physical cutting of FFPE tissue blocks in histology (i.e. microtomy), which can distort the tissue structure [49]. 3D X-ray histology data can be used as reference point to review the tissue in its initial state, prior to physical sectioning, which induces tissue distortion and defects [50]. Correlative 3D µCT-2D histology renderings can be used to assess the extent and location of tissue loss, damage, and distortion induced during

histology slide production [50-52]. More importantly, these hybrid image rendering modes provide novel and unique ways to cross-reference and analyse microstructural tissue details in 2D and interpret them in a 3D context. Co-registered histology and volumetric µCT data puts in context the conventional histology images within the 3D structure that is depicted by the µCT data. However, it is worth noting that at this stage of multimodal image fusion, co-registration of the volumetric µCT data and 2D histology required a moderate amount of data handling and manipulation (1-2 hours per dataset for this study) in specialised 3D volume manipulating software suites.

Multi-planar reconstruction (MPR)

MPR on the other hand, is a rendering mode immediately available to the user after CT reconstruction and represents a powerful 3D visualisation tool for 3D X-ray histology data. The "XY plane" image shown in Figure 5 is a virtual section, analogous to what a physical section would have generated. Consequently, scrolling through the XY image stack of virtual sections is equivalent to physical serial sectioning the tissue block to exhaustion, with a slice spacing equal to the CT voxel size (here 8 µm). Interactive image stack and orthogonal plane renderings (Supplementary Video 2 & Supplementary Video 3) of the µCT data can be used to provide a detailed overview of tissues microstructure, the histology-equivalent of which would require sectioning of the tissue block to exhaustion at huge manpower costs. For instance, a 15 mm × 15 mm-wide × 1 mm-thick piece of tissue, sectioned at a typical interval of 4 µm, would result in 250 histological sections if processed throughout its entire depth, while the same specimen can be scanned using µCT in just a few hours in 3D and at voxel size of 8 µm, resulting in more than hundred 8 µm-thick virtual sections.

As shown in Figure 5 and demonstrated in Supplementary Video 3, MPR also enables the user to dynamically adjust the slicing orientation. In a medical context this can be used for obtaining the most relevant histological (virtual) section and for examining tissue sections along all three orthogonal planes simultaneously. The resulting dataset can be used for analysing the spatial arrangements of tissue (micro)structures, their orientation as well as heterogeneity and connectivity in 3D.

From the sample preparation point of view, MPR can be exploited to preview the tissue and define the optimal physical sectioning orientation of the tissue and guide histological sectioning for conventional histology; i.e. image-guided histological sectioning [36, 53, 54]. µCT can provide information about the appropriate tissue orientation, presence or absence and location (e.g. depth) within the tissue of specific features of interest, a prospect particularly valuable in cases of small, oddly-shaped biopsies and/or applications where there is a real risk of missing the relevant tissue depth for histology (e.g. tumour margin assessment).

Maximum intensity projections (MIP)

The aforementioned MPR rendering mode adds depth information to a 2D image, by simultaneously providing the user with 2D virtual sections along the depth and width of a specific tissue feature. 3D perception is reliant upon the user's ability/training. In contrary, MIP is a 2D representation of the 3D structure. MIP selectively renders the brightest voxels, characteristic for structures with higher X-ray absorption, along a specific path, providing an overview of the spatial density of structures such as vessels, airways, calcifications or exogenous deposits. As 3D renderings with MIP are computationally inexpensive with little to no manual input, they can

provide an immediate overview of dense structures such as vessels, airway or calcifications for fast volume screening. For instance, the extent of change in the lung vascular network due to disease or anatomy can be visualised and assessed immediately as demonstrated in Figure 6. MIP rendering is widely used in radiology [55], mainly for angiography. However, MIP presentations lack true 3D depth and the viewer cannot discriminate if a certain feature is in front of behind another one, along the rendered path. This limitation can be mitigated by composing sequential MIPs of the volume at different angular positions by rotating the volume about a predefined axis (Supplementary Video 4 & Supplementary Video 5). When motion is added, for instance by dynamic spatial manipulation or video rendering, the viewer perceives depth information leading to spatial localisation of the rendered features.

Calibrated data: the key to widespread application and adoption of 3D X-ray histology

For widespread application and adoption of 3D X-ray histology, the technique must also offer calibration protocols for providing reproducible µCT image quality that guarantee comparable results over time and between different laboratories. In clinical CT this is achieved by regular quality control (QC) tests of the CT equipment, which ensure that the achieved image quality fall within an accepted tolerance depending on the application [56], both in terms of random uncertainty in voxel value (noise) and CT number (calibrated voxel grey values; see below).

In this study, we devised a calibration protocol similar to that used for calibrating clinical CT equipment, which sets the CT numbers of water at 0 and air at -1000 in the Hounsfield scale [6], but instead of water we used paraffin wax as the reference material. Hounsfield units (HU) are used for biological systems, where water constitutes the main component. The selected range of the Hounsfield scale provides a quantitative tool for assessing whether the X-ray attenuation of a given voxel in a CT volume is equal, greater (e.g. bones) or lower (e.g. fat) than water. However, FFPE specimens of soft tissues are comprised of dehydrated tissue, wax, and air, all of which exhibit lower X-ray attenuation than water. As a result, the CT numbers in a µCT image of an unstained FFPE specimen would be negative (HU < 0). By selecting the paraffin wax as reference material and by setting air to 0 (as opposed to water) ensured in the current study that the resulting grey values of the calibrated 3D X-ray histology datasets were always positive. Quantitative industrial CT often adopts a similar approach where the Hounsfield scale is offset by +1000 units and redefined such that air is 0 and water +1000 (sometimes referred to as “Industrial Hounsfield Units” or “Offset Hounsfield Units” [57, 58]).

3D Imaging: the missing link

3D imaging of tissue structures by µCT provides information about spatial heterogeneity (Figure 6 & Figure 7) and connectivity of the tissue [37], which is not accessible in 2D. The non-destructive, high-resolution capability of 3D X-ray histology also allows for whole-cassette visualisation down to microscopic levels, minimising the risk of inadequate tissue sampling. Currently, scanning volumes for a voxel size range of 5-10 µm vary from ~100-800 mm^3 using the imaging protocol presented here, however this can be significantly increased with the implementation of alternative acquisition techniques such as helical cone-beam or fan-beam µCT [59].

Disease classification for patient stratification relies on histopathologists with many years of training and experience. Despite this, diseases such as ILD with extensive tissue heterogeneity and histological variability still have poor rates of inter-observer agreement even between experts [60]. Quantitative microstructural analysis at histological resolution in 3D is likely to deliver significant added value to the interpretation of pathological changes. In addition, areas where such pathological changes are present can be located and related to their 3D context within the tissue volume. 3D X-ray histology can provide increased and novel contextual information in a multi-planar and multi-scale format. Structures with different orientations within the tissue architecture can now be viewed as 3D objects *in silico*. Pathological features and changes in tissue microstructure can be interpreted and analysed in 3D, as opposed to being limited to 2D sections, uncovering the true extent of tissue dysmorphia.

The results of the analysis presented here demonstrate that microstructural characteristics, such a tissue thickness and volume fraction, can be assessed by quantitative morphometric measures in 3D, also allowing local heterogeneity to be identified (Figure 7, Supplementary Video 6 & Supplementary Video 7). At this point it is important to note that the exemplars of local thickness and volume fraction presented in Figure 7 were used solely to demonstrate the quantitative imaging capability of the technique. While it is reasonable to assume that both these measures could differ between the control and the IPF tissue, this study was not designed to provide evidence of that. The measured difference might well be due to other factors such as difference in vascularity, presence of airways, etc.

Nonetheless, the ability to quantify 3D features adds a new family of classifiable measures, which when paired with artificial intelligent and computer-aided diagnosis systems, could potentially revolutionise diagnostics [61]. Importantly, being a non-destructive and non-contact technique, 3D X-ray histology is fully compatible with subsequent sectioning for conventional histology.

Conclusions and outlook

Current laboratory-based µCT imaging protocols for soft tissue imaging mostly rely on contrast agents and intrusive staining procedures of the tissue, which can adversely affect tissue characteristics such as immunoreactivity. This represents a significant barrier for the uptake of µCT-based 3D imaging into routine histology workflows. The ability to integrate 3D X-ray histology datasets of standard FFPE samples (Figure 1 & Figure 2) into manageable and timely analysis platforms for more rapid and systematic analysis (Figure 3, Figure 4 and Figure 6) will allow for µCT to become a routine partner in the analysis of soft tissue, both in biomedical research as well as in a medical/clinical context.

In this study, we demonstrated how the presented soft tissue-optimised µCT workflow for 3D X-ray histology can be validated by standard 2D histological techniques, opening the way for widespread application and adoption in basic research and clinical pathology. As a research tool, non-destructive 3D X-ray histology can be combined with an array of existing 2D histological techniques, including immunocytochemistry, immunofluorescence, and *in situ* hybridisation, leading to better understanding of disease initiation and progression in 3D. In pathology, 3D X-ray histology could help identifying new microstructural hallmarks of

disease. Notably, it will enable high-resolution 3D imaging to be applied to the plethora of archival FFPE material stored in many hospitals and tissue banks, which will deepen our understanding of disease progression. If combined with patient records, it will allow validation of microstructural hallmarks of disease in terms of their diagnostic and predictive power for soft tissue-related diseases using clinical endpoints. In a clinical environment, 3D X-ray histology, coupled with artificial intelligence/computer-aided diagnosis could improve diagnostic accuracy and support patient stratification.

At this stage, further work needs to be performed to define the context in which microscopic 3D volumetric analysis is useful in a medical/clinical environment. At the same time, we strongly believe that similarly to how medical CT and MRI revolutionised clinical practice in recent decades, 3D X-ray histology will play a pivotal role in research and clinical histology in the near future.

Acknowledgments

We are grateful to Mat Lawson, Sanjay Jogai, Shireen Padayachy, Gareth Thomas and Mark Mavrogordato for their input and fruitful discussion during the course of this work. We are particularly grateful to Jeffrey Myers (University of Michigan, USA), Aurelie Fabre (University College Dublin, Ireland), William Roche (University of Southampton, UK), Andrew Nicholson (Imperial College London, UK) and Alberto Cavazza (Arcispedale St. Maria Nuova, Italy) for their valuable input during the course of this project. We would also like to acknowledge the µ-VIS X-Ray Imaging Centre and the Biomedical Imaging Unit at the University of Southampton, UK for the provision of imaging, processing, and data management infrastructure, and the Histochemistry Research Unit at the University of Southampton for providing access to histology equipment. This work was supported by the Wellcome Trust (Pathfinder Award, grant number WT109682MA).

Data availability

Supplementary information is available on the online version of the paper. All data supporting this study are openly available from the University of Southampton repository at https://doi.org/ 10.5258/SOTON/D0902.

References

[1] Nicholson AG, Fulford LG, Colby TV, Du Bois RM, Hansell DM, Wells AU: The relationship between individual histologic features and disease progression in idiopathic pulmonary fibrosis. American journal of respiratory and critical care medicine 2002, 166:173-7.

[2] Hussein I, Raad M, Safa R, Jurjus RA, Jurjus A: Once Upon a Microscopic Slide: The Story of Histology. Journal of Cytology & Histology 2015, 6.

[3] Roberts N, Magee D, Song Y, Brabazon K, Shires M, Crellin D, Orsi NM, Quirke R, Quirke P, Treanor D: Toward routine use of 3D histopathology as a research tool. The American journal of pathology 2012, 180:1835-42.

[4] Tolkach Y, Thomann S, Kristiansen G: Three-dimensional reconstruction of prostate cancer architecture with serial immunohistochemical sections: hallmarks of tumour growth, tumour compartmentalisation, and implications for grading and heterogeneity. Histopathology 2018, 72:1051-9.

[5] Kawamura N, Kobayashi H, Yokota T, Hontani H, Iwamoto C, Ohuchida K, Hashizume M: Landmark-based reconstruction of 3D smooth structures from serial histological sections. International Society for Optics and Photonics. p. 105811E.

[6] Kalender WA: Computed tomography: fundamentals, system technology, image quality, applications: John Wiley & Sons, 2011.

[7] Müller R: Hierarchical microimaging of bone structure and function. Nat Rev Rheumatol 2009, 5:373-81.

[8] Miles J, Mavrogordato M, Sinclair I, Hinton D, Boardman R, Earl G: The use of computed tomography for the study of archaeological coins. Journal of Archaeological Science: Reports 2016, 6:35-41.

[9] Freeth T, Bitsakis Y, Moussas X, Seiradakis JH, Tselikas A, Mangou H, Zafeiropoulou M, Hadland R, Bate D, Ramsey A: Decoding the ancient Greek astronomical calculator known as the Antikythera Mechanism. Nature 2006, 444:587.

[10] Bouxsein ML, Boyd SK, Christiansen BA, Guldberg RE, Jepsen KJ, Müller R: Guidelines for assessment of bone microstructure in rodents using micro–computed tomography. Journal of bone and mineral research 2010, 25:1468-86.

[11] Jenkins T, Katsamenis OL, Andriotis OG, Coutts LV, Carter B, Dunlop DG, Oreffo ROC, Cooper C, Harvey NC, Thurner PJ, Grp TO: The inferomedial femoral neck is compromised by age but not disease: Fracture toughness and the multifactorial mechanisms comprising reference point microindentation. Journal of the Mechanical Behavior of Biomedical Materials 2017, 75:399-412.

[12] Metscher BD: MicroCT for comparative morphology: simple staining methods allow high-contrast 3D imaging of diverse non-mineralized animal tissues. BMC Physiol 2009, 9:11.

[13] Feldkamp LA, Goldstein SA, Parfitt MA, Jesion G, Kleerekoper M: The direct examination of three-dimensional bone architecture in vitro by computed tomography. Journal of bone and mineral research 2009, 4:3-11.

[14] Schmidt C, Priemel M, Kohler T, Weusten A, Müller R, Amling M, Eckstein F: Precision and accuracy of peripheral quantitative computed tomography (pQCT) in the mouse skeleton compared with histology and microcomputed tomography (microCT). J Bone Miner Res 2003, 18:1486-96.

[15] Zeller-Plumhoff B, Mead JL, Tan D, Roose T, Clough GF, Boardman RP, Schneider P: Soft tissue 3D imaging in the lab through optimised propagation-based phase contrast computed tomography. Optics Express 2017, 25:33451-68.

[16] Muller R, Van Campenhout H, Van Damme B, Van Der Perre G, Dequeker J, Hildebrand T, Rüegsegger P: Morphometric analysis of human bone biopsies: a quantitative structural comparison of histological sections and micro-computed tomography. Bone 1998, 23:59-66.

[17] Neues F, Epple M: X-ray microcomputer tomography for the study of biomineralized endo- and exoskeletons of animals. Chem Rev 2008, 108:4734-41.

[18] Corni I, Symonds N, Birrell CE, Katsamenis OL, Wasenczuk A, Vincent D: Characterization and mapping of rolling contact fatigue in rail-axle bearings. Engineering Failure Analysis 2017, 82:617-30.

[19] Keyes SD, Gillard F, Soper N, Mavrogordato MN, Sinclair I, Roose T: Mapping soil deformation around plant roots using in vivo 4D X-ray Computed Tomography and Digital Volume Correlation. J Biomech 2016, 49:1802-11.

[20] Sinnett-Jones PE, Browne M, Ludwig W, Buffière JY, Sinclair I: Microtomography assessment of failure in acrylic bone cement. Biomaterials 2005, 26:6460-6.

[21] Gillard F, Boardman R, Mavrogordato M, Hollis D, Sinclair I, Pierron F, Browne M: The application of digital volume correlation (DVC) to study the microstructural behaviour of trabecular bone during compression. J Mech Behav Biomed Mater 2014, 29:480-99.

[22] Barker CT, Naish D, Newham E, Katsamenis OL, Dyke G: Complex neuroanatomy in the rostrum of the Isle of Wight theropod Neovenator salerii. Scientific Reports 2017, 7:3749.
[23] Lessner EJ, Stocker MR: Archosauriform endocranial morphology and osteological evidence for semiaquatic sensory adaptations in phytosaurs. J Anat 2017, 231:655-64.
[24] Stauber M, Müller R: Micro-computed tomography: a method for the non-destructive evaluation of the three-dimensional structure of biological specimens. Osteoporosis: Springer, 2008. pp. 273-92.
[25] Metscher BD: MicroCT for developmental biology: a versatile tool for high-contrast 3D imaging at histological resolutions. Dev Dyn 2009, 238:632-40.
[26] Ritman EL: Micro-computed tomography—current status and developments. Annu Rev Biomed Eng 2004, 6:185-208.
[27] Mizutani R, Suzuki Y: X-ray microtomography in biology. Micron 2012, 43:104-15.
[28] Jeffery NS, Stephenson RS, Gallagher JA, Jarvis JC, Cox PG: Micro-computed tomography with iodine staining resolves the arrangement of muscle fibres. Journal of biomechanics 2011, 44:189-92.
[29] Zeller-Plumhoff B, Roose T, Katsamenis OL, Mavrogordato MN, Torrens C, Schneider P, Clough GF: Phase contrast synchrotron radiation computed tomography of muscle spindles in the mouse soleus muscle. Journal of Anatomy 2017, 230:859-65.
[30] Zehbe R, Riesemeier H, Kirkpatrick CJ, Brochhausen C: Imaging of articular cartilage–Data matching using X-ray tomography, SEM, FIB slicing and conventional histology. Micron 2012, 43:1060-7.
[31] Pauwels E, Van Loo D, Cornillie P, Brabant L, Van Hoorebeke L: An exploratory study of contrast agents for soft tissue visualization by means of high resolution X-ray computed tomography imaging. J Microsc 2013, 250:21-31.
[32] Albers J, Pacilé S, Markus MA, Wiart M, Velde GV, Tromba G, Dullin C: X-ray-Based 3D Virtual Histology—Adding the Next Dimension to Histological Analysis. Molecular Imaging and Biology 2018:1-10.
[33] Pauwels E, Van Loo D, Cornillie P, Brabant L, Van Hoorebeke L: An exploratory study of contrast agents for soft tissue visualization by means of high resolution X-ray computed tomography imaging. Journal of microscopy 2013, 250:21-31.
[34] Balint R, Lowe T, Shearer T: Optimal contrast agent staining of ligaments and tendons for X-ray computed tomography. PloS one 2016, 11:e0153552.
[35] Vickerton P, Jarvis J, Jeffery N: Concentration-dependent specimen shrinkage in iodine-enhanced micro CT. Journal of anatomy 2013, 223:185-93.
[36] Scott AE, Vasilescu DM, Seal KA, Keyes SD, Mavrogordato MN, Hogg JC, Sinclair I, Warner JA, Hackett TL, Lackie PM: Three dimensional imaging of paraffin embedded human lung tissue samples by micro-computed tomography. PLoS One 2015, 10:e0126230.
[37] Jones MG, Fabre A, Schneider P, Cinetto F, Sgalla G, Mavrogordato M, Jogai S, Alzetani A, Marshall BG, O'Reilly KM, Warner JA, Lackie PM, Davies DE, Hansell DM, Nicholson AG, Sinclair I, Brown KK, Richeldi L: Three-dimensional characterization of fibroblast foci in idiopathic pulmonary fibrosis. JCI Insight 2016, 1.
[38] Cool CD, Groshong SD, Rai PR, Henson PM, Stewart JS, Brown KK: Fibroblast foci are not discrete sites of lung injury or repair: The fibroblast reticulum. Am J Respir Crit Care Med 2006, 174:654-8.
[39] Schindelin J, Arganda-Carreras I, Frise E, Kaynig V, Longair M, Pietzsch T, Preibisch S, Rueden C, Saalfeld S, Schmid B, Tinevez J-Y, White DJ, Hartenstein V, Eliceiri K, Tomancak P, Cardona A: Fiji: an open-source platform for biological-image analysis. Nature Methods 2012, 9:676.
[40] Schneider CA, Rasband WS, Eliceiri KW: NIH Image to ImageJ: 25 years of image analysis. Nat Methods 2012, 9:671-5.
[41] Sorzano COS, Thévenaz P, Unser M: Elastic registration of biological images using vector-spline regularization. IEEE Transactions on Biomedical Engineering 2005, 52:652-63.
[42] Sorzano CO, Thévenaz P, Unser M: Elastic registration of biological images using vector-spline regularization. IEEE Trans Biomed Eng 2005, 52:652-63.
[43] Loraine Lowder M, Li S, Carnell PH, Vito RP: Correction of distortion of histologic sections of arteries. J Biomech 2007, 40:445-50.
[44] Rastogi V, Puri N, Arora S, Kaur G, Yadav L, Sharma R: Artefacts: a diagnostic dilemma–a review. Journal of clinical and diagnostic research: JCDR 2013, 7:2408.
[45] Doube M, Klosowski MM, Arganda-Carreras I, Cordelieres FP, Dougherty RP, Jackson JS, Schmid B, Hutchinson JR, Shefelbine SJ: BoneJ: Free and extensible bone image analysis in ImageJ. Bone 2010, 47:1076-9.
[46] Hildebrand T, Rüegsegger P: A new method for the model-independent assessment of thickness in three-dimensional images. J Microsc-Oxford 1997, 185:67-75.
[47] van Ooijen PM, Ho KY, Dorgelo J, Oudkerk M: Coronary artery imaging with multidetector CT: visualization issues. Radiographics 2003, 23:e16.

[48] Richeldi L, Collard HR, Jones MG: Idiopathic pulmonary fibrosis. The Lancet 2017, 389:1941-52.
[49] Lesson T, Lesson C, Paparo A: Text book and atlas of histology. WB Saunders Co Philadelphia 1988:195-228.
[50] Senter-Zapata M, Patel K, Bautista PA, Griffin M, Michaelson J, Yagi Y: The Role of Micro-CT in 3D Histology Imaging. Pathobiology 2016, 83:140-7.
[51] Mourad C, Laperre K, Halut M, Galant C, Van Cauter M, Berg BCV: Fused micro-computed tomography (µCT) and histological images of bone specimens. Diagnostic and interventional imaging 2018.
[52] Walton LA, Bradley RS, Withers PJ, Newton VL, Watson RE, Austin C, Sherratt MJ: Morphological characterisation of unstained and intact tissue micro-architecture by X-ray computed micro- and nano-tomography. Sci Rep 2015, 5:10074.
[53] Sengle G, Tufa SF, Sakai LY, Zulliger MA, Keene DR: A correlative method for imaging identical regions of samples by micro-CT, light microscopy, and electron microscopy: imaging adipose tissue in a model system. Journal of Histochemistry & Cytochemistry 2013, 61:263-71.
[54] Khimchenko A, Deyhle H, Schulz G, Schweighauser G, Hench J, Chicherova N, Bikis C, Hieber SE, Müller B: Extending two-dimensional histology into the third dimension through conventional micro computed tomography. NeuroImage 2016, 139:26-36.
[55] Fishman EK, Ney DR, Heath DG, Corl FM, Horton KM, Johnson PT: Volume rendering versus maximum intensity projection in CT angiography: what works best, when, and why. Radiographics 2006, 26:905-22.
[56] Bissonnette JP, Balter PA, Dong L, Langen KM, Lovelock DM, Miften M, Moseley DJ, Pouliot J, Sonke JJ, Yoo S: Quality assurance for image-guided radiation therapy utilizing CT-based technologies: a report of the AAPM TG-179. Medical physics 2012, 39:1946-63.
[57] Kisner SJ, States) PUU, Haneda E, States) PUU, Bouman CA, States) PUU, Skatter S, Morpho Detection IUS, Kourinny M, Morpho Detection IUS, Bedford S, Astrophysics IUS: Limited view angle iterative CT reconstruction. Computational Imaging X: International Society for Optics and Photonics, 2018. p. 82960F.
[58] X-TEK: CT Pro 3D User Manual (v. XT 5.1.4.3 MedX 1). Nikon Metrology, Tring Business Centre, Hertfordshire, United Kingdom: Nikon Metrology, UK, 2017.
[59] Hu H: Multi-slice helical CT: Scan and reconstruction. Medical physics 1999, 26:5-18.
[60] Kaarteenaho R: The current position of surgical lung biopsy in the diagnosis of idiopathic pulmonary fibrosis. Respiratory research 2013, 14:43.
[61] Bueno G, Fernández-Carrobles MM, Deniz O, García-Rojo M: New trends of emerging technologies in digital pathology. Pathobiology 2016, 83:61-9.

Figure captions

Figure 1

High-resolution medical CT, "3D X-ray histology" using µCT and conventional histology. In lung pathology, anatomical imaging is performed by high-resolution medical CT (left panel), whereas cellular analysis is conducted by conventional histology (right panel). µCT imaging (middle panel) bridges the gap between these traditional imaging modalities, allowing for 3D analysis of biopsy samples at microscopic resolutions. *source: Jones *et al*. [37], #source: Wikimedia commons (Mikael Häggström).

Figure 2

Workflow for 3D µCT imaging and conventional 2D histology. The figure demonstrates the added value of non-destructive 3D imaging to the conventional workflow of tissue analysis by light microscopy, providing high-resolution 3D data that can be integrated seamlessly into protocols for conventional 2D histology.

Figure 3

Comparison between lung tissue imaged by µCT and light microscopy for conventional histology. The lung biopsy sample has been taken from a non-involved site from a patient with lung cancer. The µCT slice is provided in panels A, B, and C and the digitised image of the histology slide in panels C, D, and F; labelled insets in A, B, D, and E define the areas shown at higher magnification levels in the panels immediately to the right. The histology image in D is intentionally presented against a grey background to highlight the degree to which the image had to be unwrapped to fit its non-distorted state (i.e. before sectioning). The comparison shows that tissue lung microstructure is clearly visible in the µCT dataset at high contrast levels, which is due to the newly developed µCT scanner that is optimised for soft tissue imaging at high spatial resolutions. Higher magnification images (middle and right panel, with boxes indicating enlarged areas of interest) are also provided for comparison of µCT imaging to the higher resolution light microscopy histology. Arrows and octothorpe on sub-panels C and F indicate an airway and a blood vessel. Scale bar in A: 2 mm, B: 1 mm, and C: 500 µm.

Figure 4

Hybrid visualisation of conventional 2D histology slide and 3D X-ray histology image data. Control tissue (left) and tissue from patient with interstitial lung disease (IPF) (right). Sub-sections (red box: 2.4 mm × 2.4 mm) of the tissue imaged by µCT were extracted and cubic sub-volumes (blue box: 1.2 mm × 1.2 mm × 1.2 mm) rendered that protrude above this surface. Co-registered 2D histology sections are placed on top of the rendered µCT cubes at their correct tissue depth, highlighting the capability to combine or fuse conventional 2D histology slides and 3D X-ray histology data. 3D alveolar structure in control lung (left) can be directly compared to microstructural changes induced by IPF (right).

Figure 5

Multi-planar reconstruction (MPR) of 3D X-ray histology data. (Top row) 3D X-ray histology images can be reviewed immediately following CT reconstruction as an interactive image stack in the three principal orthogonal planes, with the "XY plane" defined (by convention) as the plane parallel to histology cassette. In this 2D view,

609 the observer can browse through the depth, width and height of the specimen, zoom, pan, and perform
610 dimensional measurements. The uneven surface of the untrimmed wax can be seen as bright edge at the bottom
611 of the images shown in the “YZ plane” and “XZ plane”. (Middle & bottom row) Examples of re-orientation and
612 re-slicing of the specimen to obtain the most relevant histological (virtual) section. The process can be repeated
613 on the fly for multiple features, and as many times as required.

614 ## Figure 6

615 **Maximal intensity projections of 3D X-ray histology data**. Control tissue (left) and tissue from patient with
616 interstitial lung disease (IPF) (right). Snapshots of 3D volumes are shown as maximum intensity projections
617 (MIPs). MIP rendering consists of projecting the pixels with the highest X-ray attenuation, which helps to discern
618 denser features such as the vascular network from the surrounding tissue, without the need of data
619 segmentation. MIPs illustrate a clear difference between the vascular network in control tissue (left) and ablated
620 vascular structures observed for the IPF lung tissue (right). Samples were of equivalent size, and identical
621 threshold parameters were applied for both samples. Scale bars: 2 mm.

622 ## Figure 7

623 **Quantitative analysis of the tissue thickness**. Analysis of the local tissue thickness showing the differences
624 between the volumetric characteristics of control and the IPF tissue biopsy. On average, control lung tissue was
625 comprised of finer elements with an average thickness of 42 µm (~5 pixels sphere diameter at a voxel size of
626 8.48 µm), compared to much thicker elements for the IPF tissue biopsy with an average thickness of 127 µm
627 (~15 pixels). The histogram on the left panel depicts the frequency and distribution of all tissue voxels (3D pixels)
628 based on the thickness of the element they belong to. The graph also presents the calculated average (mean)
629 thickness for each specimen (dashed vertical lines), along with the associated standard deviation (solid line
630 whiskers). The panel on the right is a volume rendering of the thickness map for both specimens. Both colour
631 maps are to scale and range from 0 µm (black/blue) to 300 µm (yellow). This view provides a complementary
632 qualitative visualisation of the thickness heterogeneity.

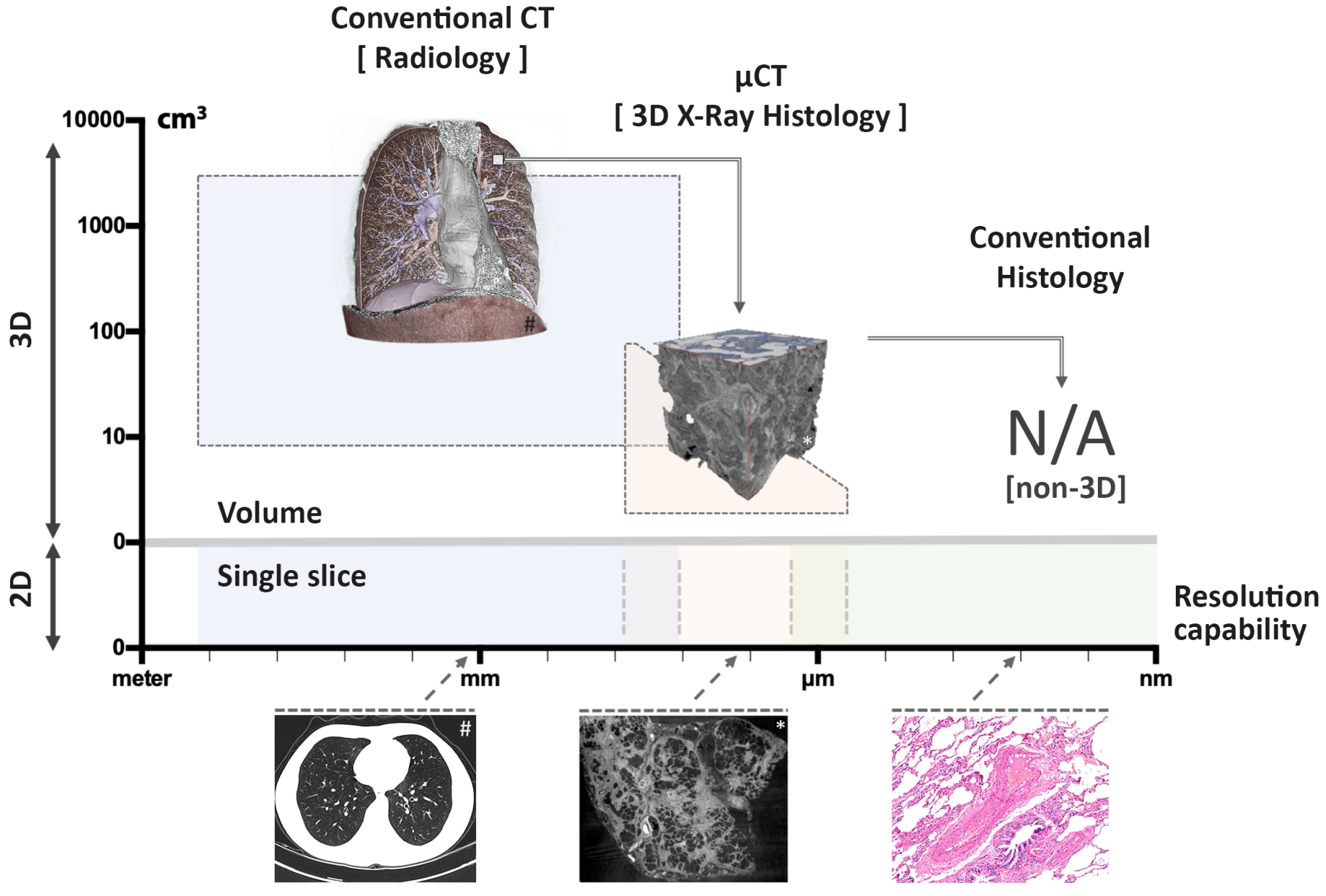
Conventional CT
[Radiology]
µCT
[3D X-Ray Histology]
Conventional
Histology
10000
cm³
1000
100
10
0
0
3D
2D
Volume
Single slice
N/A
[non-3D]
Resolution
capability
meter
mm
µm
nm
#
*

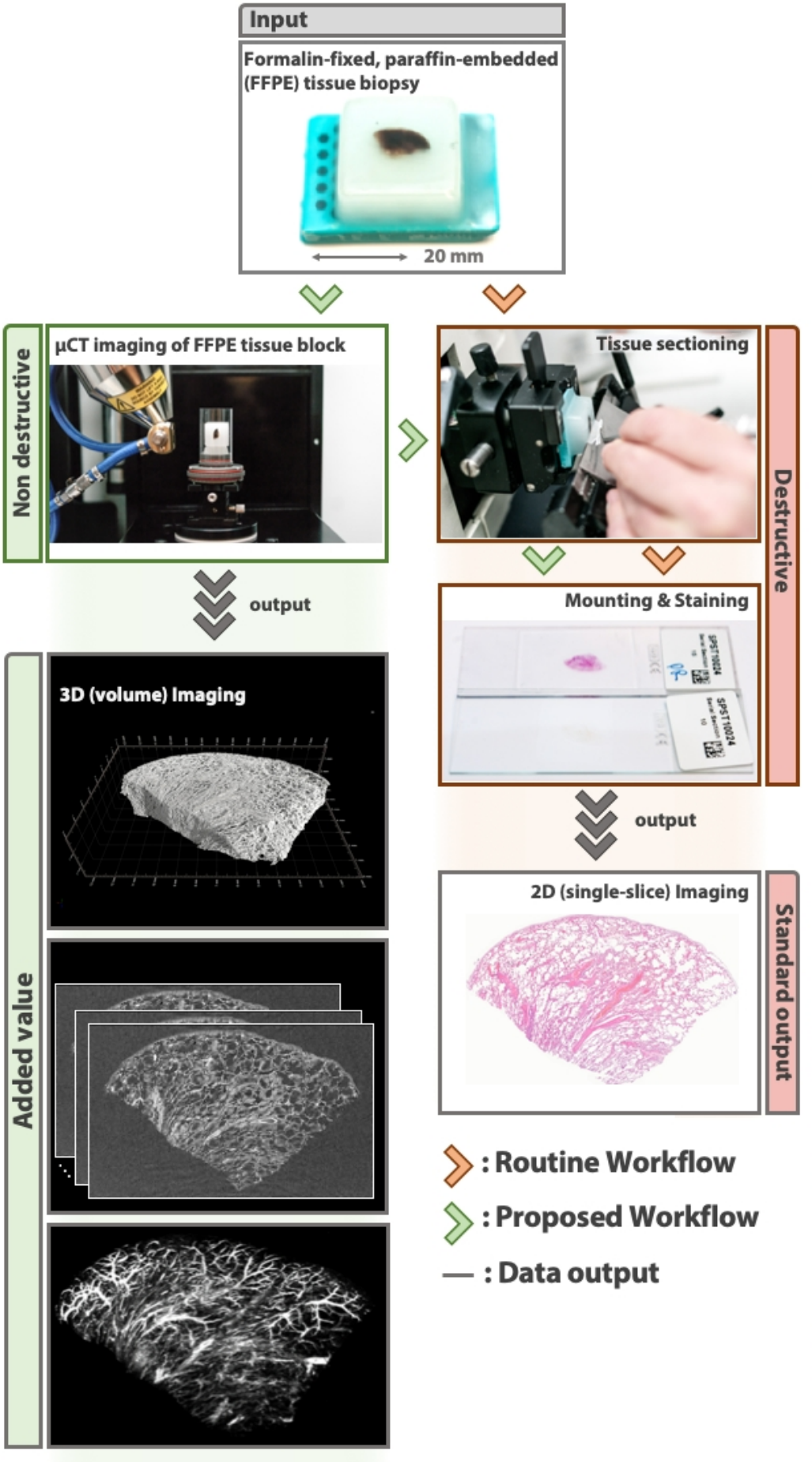
Input
Formalin-fixed, paraffin-embedded (FFPE) tissue biopsy
20 mm
Non destructive
µCT imaging of FFPE tissue block
Tissue sectioning
Destructive
output
Mounting & Staining
output
Added value
3D (volume) Imaging
2D (single-slice) Imaging
Standard output
: Routine Workflow
: Proposed Workflow
: Data output

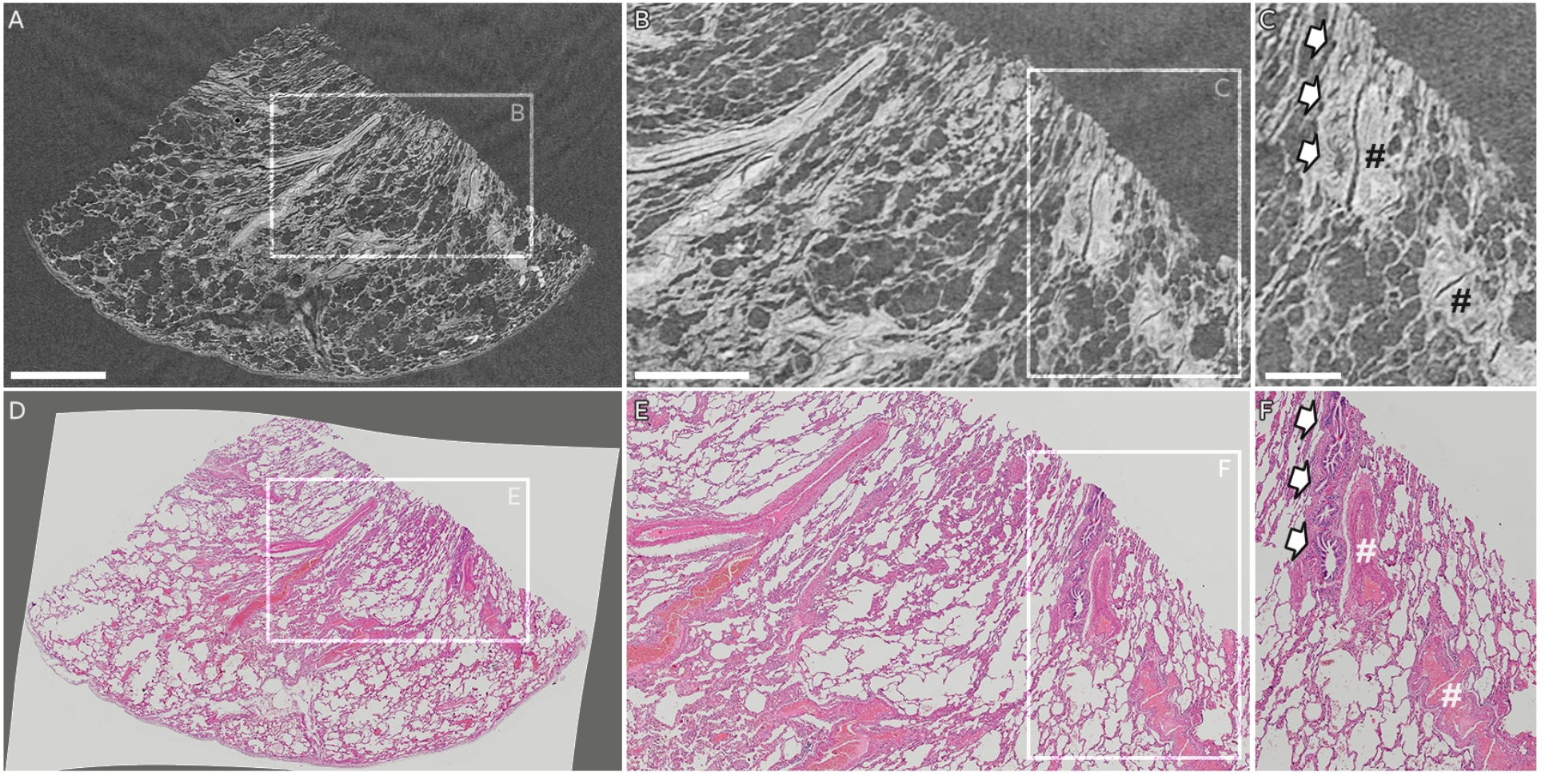
A
B
B
C
C
#
#
D
E
E
F
F
#
#

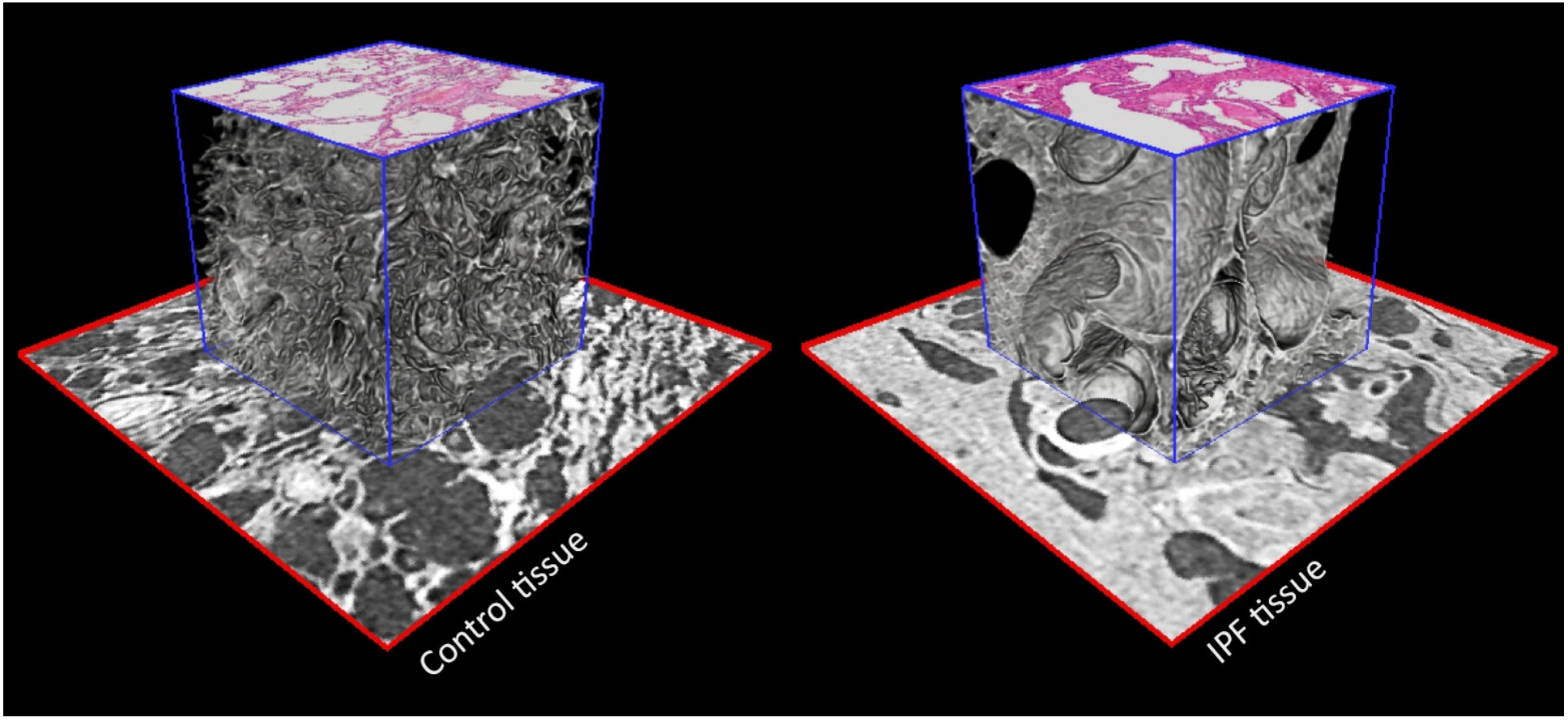
Control tissue
IPF tissue

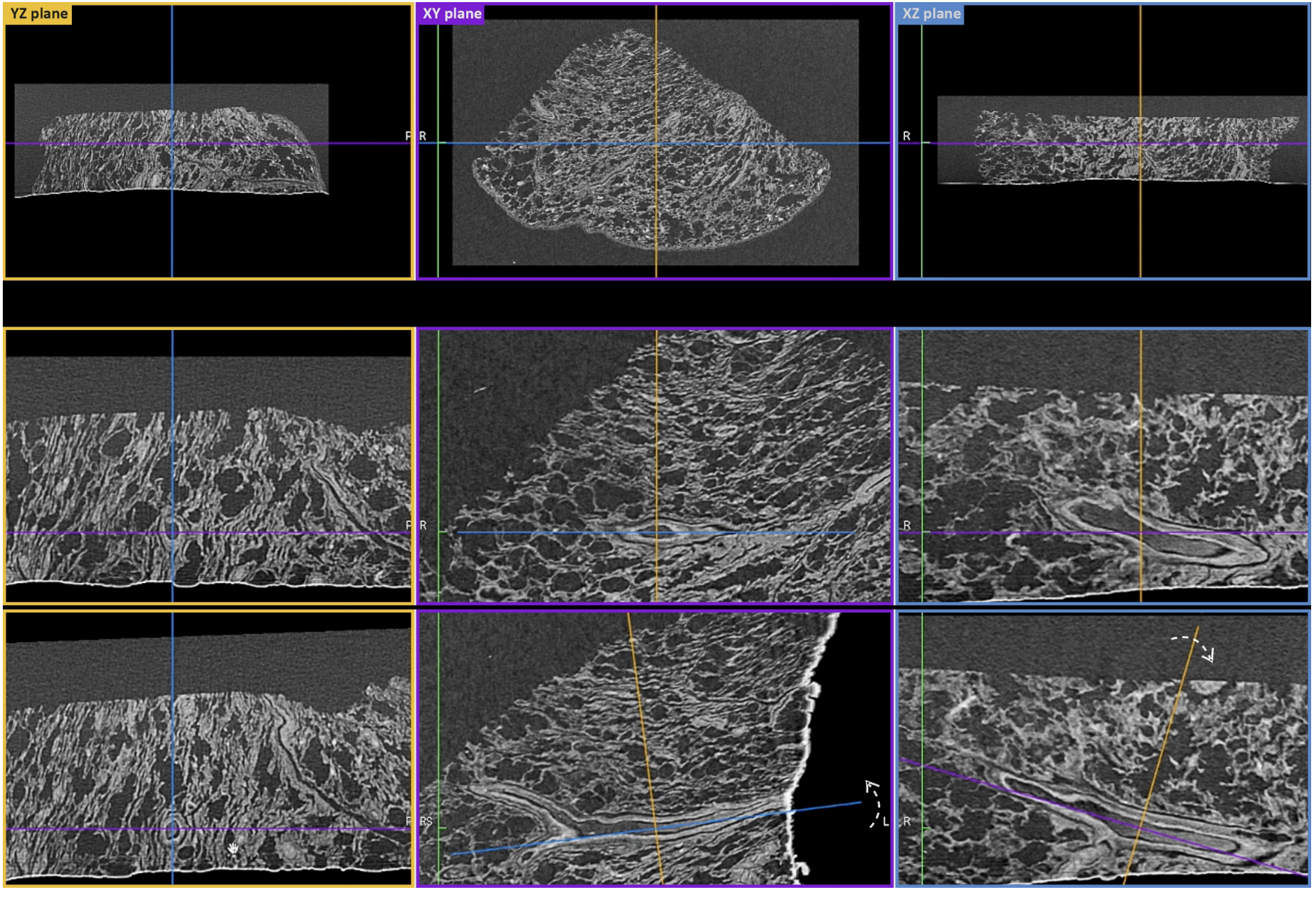
YZ plane
XY plane
XZ plane
P
R
R
R
P
R
R
P
R
S
L
R

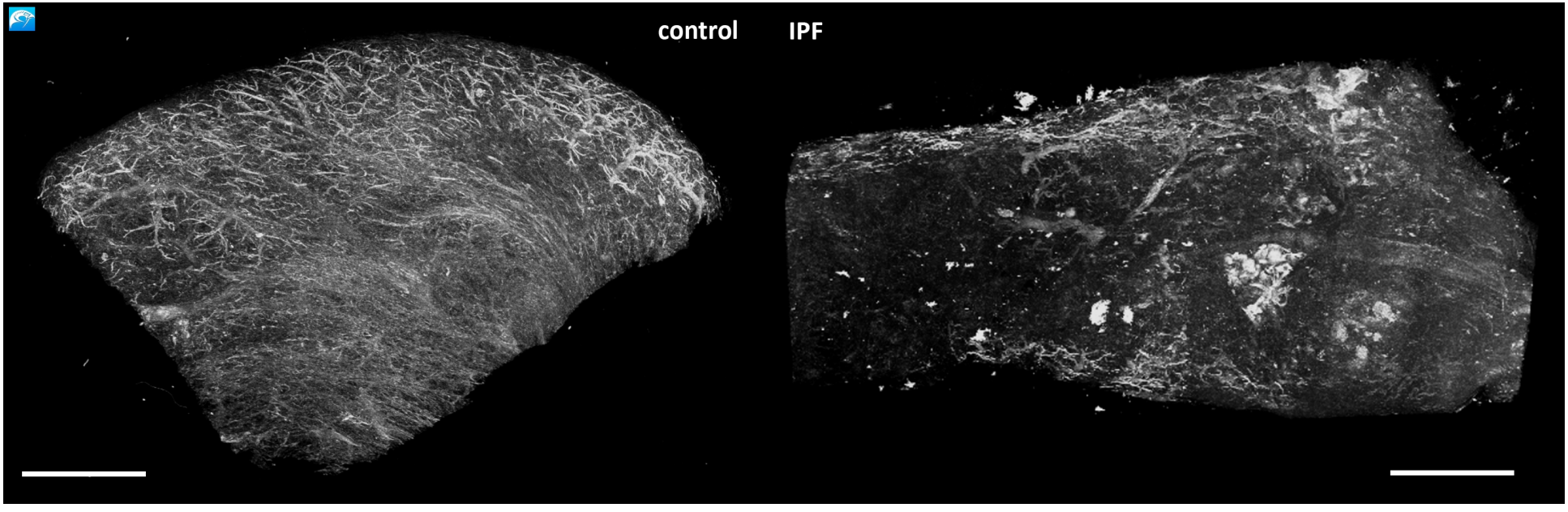
control
IPF

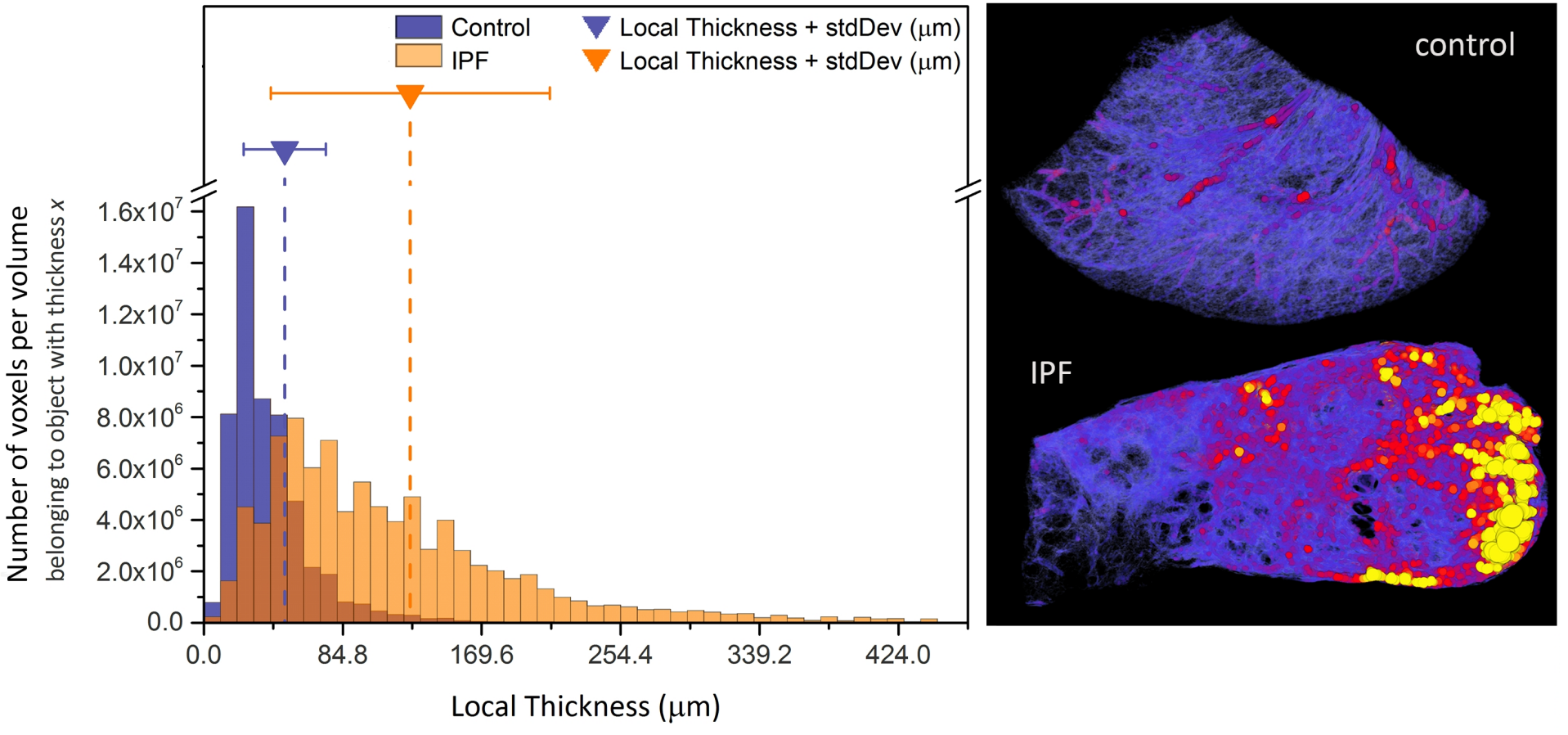
Control
IPF
Local Thickness + stdDev (μm)
Local Thickness + stdDev (μm)
Number of voxels per volume
belonging to object with thickness x
1.6x10^7
1.4x10^7
1.2x10^7
1.0x10^7
8.0x10^6
6.0x10^6
4.0x10^6
2.0x10^6
0.0
0.0
84.8
169.6
254.4
339.2
424.0
Local Thickness (μm)
control
IPF

X-ray micro-computed tomography for non-destructive 3D X-ray histology: Supplementary material

Authors

Orestis L. Katsamenis[1*♦], Michael Olding[2+♦], Jane A. Warner[3], David S. Chatelet[2], Mark G. Jones[4], Giacomo Sgalla[4±], Bennie Smit[5], Oliver J. Larkin[5], Ian Haig[5], Luca Richeldi[4], Ian Sinclair[1,6], Peter M. Lackie[2,3], Philipp Schneider[1,7*]

* *Corresponding authors*

♦ *Orestis L. Katsamenis and Michael Olding contributed equally to this work*

Affiliations

[1] µ-VIS X-Ray Imaging Centre, Faculty of Engineering and Physical Sciences, University of Southampton, UK

[2] Biomedical Imaging Unit, Clinical & Experimental Sciences, Faculty of Medicine, University of Southampton, Southampton General Hospital, Southampton, UK

[3] Academic Unit of Clinical and Experimental Sciences, Faculty of Medicine, University of Southampton, Southampton, UK

[4] National Institute for Health Research Respiratory Biomedical Research Unit, University Hospital, Southampton, Southampton, UK

[5] Nikon X-Tek Systems Ltd, Tring Business Centre, Icknield Way, HP23 4JX Tring, Herts, UK

[6] Engineering Materials Research Group, Faculty of Engineering and Physical Sciences, University of Southampton, Southampton, UK

[7] Bioengineering Science Research Group, Faculty of Engineering and Physical Sciences, University of Southampton, Southampton, UK

[+] current address: Nikon X-Tek Systems Ltd, Tring Business Centre, Icknield Way, HP23 4JX Tring, Herts, UK

[±] current address: Dipartimento di Scienze Cardiovascolari e Toraciche, Fondazione Policlinico Universitario A. Gemelli IRCCS, Rome, Italy

Supplementary material

Supplementary Figure 1

Stability of the new µCT scanner for 3D X-ray histology. (Left panel) Grey value variation for both the paraffin wax (purple) and lung tissue material (green) of 30 scans (not shown in this study) after calibration, spanning a 3-months µCT imaging period. (Right panel) Raw 16-bit histograms (black line) of central slices of nine representative specimens spanning the duration of the aforementioned period, together with the corresponding fitted (Gaussian) peaks for the wax (purple) and tissue material (green) after calibration.

Supplementary Video 1

Simultaneous visualisation of single µCT and H&E histology slice. Co-registration of histology with µCT image data and simultaneous visualisation of both datasets allows for direct comparison of the two imaging modalities and precise, histology-guided identification of a wide range of tissue structures and diagnostically relevant histological criteria. Visualisation platform: Horos™ (v2.0.2; https://horosproject.org).

Supplementary Video 2

Scrolling through XY slice-stack (i.e. virtual sectioning). µCT data can be reviewed immediately following CT reconstruction. In its simplest case, volume visualisation is accomplished within seconds after µCT scan completion on a slice-by-slice basis, presented as an interactive image stack in which the viewer can browse through the depth of the specimen, zoom, pan, and conduct dimensional measurements. Visualisation platform: Horos™ (v2.0.2).

Supplementary Video 3

Orthogonal planes view & arbitrary virtual slicing. Orthogonal planes of the µCT data can also be viewed immediately after CT reconstruction for analysing the spatial arrangements of tissue (micro)structures, their orientation as well as heterogeneity and connectivity in (3D) space. An example of such an interactive assessment of 3D data is shown here, where the reviewer locates blood vessel and examines the cross-sectional views along two orthogonal planes. Visualisation platform: Horos™ (v2.0.2).

Supplementary Video 4

Maximum intensity projection (MIP) rendering of the control lung tissue biopsy. This 2D representation of a 3D structure provides a good definition of denser structures such as vessels, airways, calcifications or exogenous deposits. MIP rendering helps identifying and emphasising particular tissue structures of interest, such as the vascular network. Dynamic MIP rendering for different angular positions (e.g. rotating video) conveys qualitative depth information to the observer. Visualisation platform: Horos™ (v2.0.2).

Supplementary Video 5

Maximum intensity projection (MIP) rendering of a lung biopsy sample obtained from a patient with idiopathic pulmonary fibrosis (IPF). This 2D representation of a 3D structure shows good definition of denser structures such as vessels, airways, calcifications or exogenous deposits. MIP rendering helps identifying and emphasising particular tissue structures of interest, such as the vascular network. Dynamic MIP rendering for

different angular positions (e.g. rotating video) conveys qualitative depth information to the human observer. Visualisation platform: Horos™ (v2.0.2).

Supplementary Video 6

3D rendering of local thickness of the control lung tissue biopsy. The video presents an overview of the 3D distribution of the local thickness of the control lung tissue biopsy. Each point is coloured according to the size of the diameter of the largest sphere that fits inside the structure at this point. Smaller elements of the structure are represented with cooler colours and bigger ones with warmer colours. The colour scale is kept consistent between this video and Supplementary Video 7.

Supplementary Video 7

3D rendering of local thickness of the IPF lung tissue biopsy. The video presents an overview of the 3D distribution of the local thickness of the IPF lung tissue biopsy. Each point is coloured according to the size of the diameter of the largest sphere that fits inside the structure at this point. Smaller elements of the structure are represented with cooler colours and bigger ones with warmer colours. The colour scale is kept consistent between this video and Supplementary Video 6.